PCCP

ROYAL SOCIETY OF CHEMISTRY

PAPER

View Article Online
View Journal | View Issue

Cite this: *Phys. Chem. Chem. Phys.*, 2024, **26**, 12672

A first-principles study on Ni-decorated MoS_2 for efficient formaldehyde degradation over a wide temperature range†

Jiahui Tang, Xiaocha Wang, Honggang Pan* and Baozeng Zhou *

The development of a high-efficiency, low-cost, and environmentally friendly catalyst for formaldehyde degradation is crucial for addressing the issue of indoor formaldehyde pollution. Given that modern individuals spend over 90% of their time indoors, effectively tackling indoor formaldehyde pollution holds significant importance. Therefore, this paper proposes an efficient catalyst for formaldehyde degradation: surface modification of MoS_2 by single-atom Ni, which can convert formaldehyde into harmless H_2O and CO_2. The DFT method is employed to systematically investigate the oxidative degradation pathways of formaldehyde on the surface of Ni-doped MoS_2. The research focuses on two common oxidative degradation pathways in both the L–H mechanism and E–R mechanism. Our findings demonstrate that these four reaction paths occur spontaneously within the temperature range of 300–800 K with a reaction equilibrium constant greater than 10^5. Moreover, even under extreme temperature conditions (100 K), the reaction rate remains favorable. Furthermore, our findings indicate that the minimum activation energy is merely 0.91 eV and H_2O and CO_2 only need to overcome an energy barrier of 0.71 eV for desorption from the catalyst surface. This substantiates its potential application both in indoor environments and under extreme temperature conditions. This theoretical research provides innovative ideas and strategies for effectively oxidizing formaldehyde.

Received 16th January 2024,
Accepted 28th March 2024

DOI: 10.1039/d4cp00189c

rsc.li/pccp

1. Introduction

Formaldehyde (HCHO) serves as a crucial feedstock for industrial production, and sophisticated methodologies to synthesize HCHO from methanol exist.[1] But for everyday life, despite its colorless and odorless nature, HCHO, as one of the simplest aldehydes, should not be underestimated due to its potential harm.[2,3] In June 2004, the International Agency for Research on Cancer (IARC) of the World Health Organization upgraded it to a Group 1 carcinogen.[4] According to Zinn *et al.*, commonly used furniture adhesives and solid wood panels along with other home improvement materials currently contain high concentrations of HCHO,[5,6] and it takes several years for this HCHO to be fully released naturally.[7] Given that modern individuals spend approximately 90% of their daily time indoors, indoor HCHO concentration directly impacts indoor air quality and our health.[8] Even prolonged exposure to low doses of HCHO can result in chronic poisoning and lead to respiratory, nervous system, and reproductive diseases. Medical research indicates that children are more susceptible to the effects of HCHO. Indoor HCHO and other harmful gases are significant contributors to leukemia.[9,10]

Due to the significant harm HCHO poses to human health, particularly in children, and its prolonged natural release time, reducing indoor HCHO concentration has become a prominent concern. The inhibition of the catalytic degradation rate of HCHO at low temperatures poses a challenge in achieving efficient degradation under extreme temperature conditions, thus warranting further investigation, the successful achievement of room temperature oxidative degradation of HCHO has been made possible through the relentless efforts of numerous scholars.[11,12] Therefore, it is crucial to employ various means of HCHO treatment. Currently, commonly used methods for treating HCHO can be categorized into four groups: (i) increased ventilation, which is one of the most commonly employed methods for reducing indoor HCHO concentrations, has been proposed by Sherman *et al.* to estimate indoor ventilation frequency based on indoor HCHO concentration.[13] However, this method is time-consuming and highly influenced by environmental factors. (ii) Surface coating involves utilizing the intense chemical reaction between HCHO and amines to produce hexamethylenetetramine as an effective and long-lasting solution for removing HCHO.[14,15]

Tianjin Key Laboratory of Film Electronic & Communicate Devices, School of Integrated Circuit Science and Engineering, Tianjin University of Technology, Tianjin 300384, China. E-mail: phg022@163.com, baozeng@tju.edu.cn

† Electronic supplementary information (ESI) available. See DOI: https://doi.org/10.1039/d4cp00189c

Nevertheless, it should be noted that the resulting hexamethylenetetramine powder can also pose harm to human health. (iii) Photocatalysis entails treating indoor aldehydes through photocatalytic oxidation using photocatalyst coatings like TiO_2.[16–19] According to the research findings of Benz *et al.*, there may be a secondary pollution risk caused by the reaction between styrene and photocatalysts leading to the production of HCHO.[20,21] (iv) Adsorption techniques involve employing plants or various adsorption materials for capturing and storing HCHO.[22,23] However, the research results of Schmitz *et al.* indicate that such methods have limited effectiveness in reducing indoor HCHO concentrations.[22] In recent years, MnO_2 has emerged as a promising catalyst for indoor HCHO treatment due to its exceptional catalytic activity and ease of preparation.[24,25] The effectiveness and safety of these methods in reducing indoor HCHO concentration are limited. However, a recent approach involving catalytic oxidation of HCHO using metals to break the C–H bond and convert it into H_2O and CO_2 has gained attention. This treatment method offers true decomposition of HCHO without causing secondary pollution, making it an excellent solution for HCHO treatment.[26–28]

The utilization of noble metals in the domain of HCHO catalytic oxidation exhibits remarkable performance. However, their extensive production and application have been hindered by cost and stability concerns.[26] The focus of HCHO degradation research has thus shifted to low-cost, resource-abundant transition metals in recent years, particularly post-transition metals with a higher number of d-band electrons.[29,30] The low catalytic oxidation activity of transition metals is an undeniable fact, thus enhancing their catalytic oxidation activity has become the foremost challenge in utilizing them for HCHO degradation. The two-dimensional semiconductor materials, such as graphene, silicene, MoS_2, *etc.*, possess a significantly large specific surface area and exhibit remarkable appeal in the realm of catalytic oxidation.[31–33] However, the catalytic activity of these materials solely originates from the unsaturated coordination atoms at their edges while a substantial number of saturated coordination atoms in their centers remain uninvolved in the catalytic reaction.[34] Consequently, this diminishes their advantage in terms of specific surface area and compromises their overall catalytic performance.[35] The construction of single-atom catalysts (SACs) represents a novel approach to enhance the abundance of active sites on the catalyst surface and enables the dispersion and anchored metal ions onto the substrate surface, resulting in uniformly distributed active sites. Consequently, it significantly augments the number of active sites on the substrate surface while affording catalysts with remarkable catalytic stability, adjustable activity, low-cost, and high durability.[36–38] According to theoretical calculations and experiments, the surface modification of MoS_2 by single transition metal atoms can take full advantage of its large specific surface area, maximize the number of active sites, and significantly improve the catalytic performance.[38,39] The hydrothermal method enables the preparation of Ni–MoS_2 nanoflowers with a large specific surface area and enhanced structural stability.[40] The laboratory preparation of Ni single-atom loaded 1T-MoS_2 is achieved through the intercalation of organic molecules, as demonstrated by Wang *et al.*[41] The successful implementation of the wet deposition technique by Hai *et al.* has facilitated the large-scale synthesis of single-atom catalysts, thereby establishing a robust foundation for their widespread production and practical applications.[42]

In this work, the catalytic degradation mechanism of HCHO on the Ni–MoS_2 surface is investigated using the DFT method. Firstly, by analyzing the adsorption characteristics of the final products of HCHO and O_2 on the Ni–MoS_2 surface, we determine the initial configuration of the catalytic degradation pathway for HCHO. The four common degradation pathways of HCHO are subsequently selected, with two for the L–H mechanism and two for the E–R mechanism. The energy changes and reaction energy barriers are then calculated to determine the rate-determining steps. Finally, based on the kinetic and thermodynamic characteristics, as well as the energy changes and reaction energy barriers observed along each pathway, predictions are made regarding variations in reaction rates at different temperatures. These analyses provide evidence of the significant potential of Ni–MoS_2 as a catalyst for HCHO degradation over a wide temperature range.

2. Calculation details

The present study employs the Vienna Ab initio Simulation Package (VASP)[43,44] to perform first-principles calculations based on density functional theory (DFT). To ensure the reliability of the results, all calculations are performed using the well-established projection enhanced wave (PAW) method to account for electron–ion correlation.[45] The PBE-GGA functional has been shown to provide a more precise description of weak correlations,[46] and previous research has also showcased the efficacy of the functional in assessing the performance of SACs.[47–49] So the Perdew-–Burke-–Ernzerhof (PBE) form of the Generalized Gradient Approximation (GGA) is employed to describe exchange and correlation effects.[43,50] Based on previous research findings, a plane wave cutoff energy of 500 eV is considered sufficient to ensure the reliability of the calculated results. In order to acquire a more accurate determination of the energy barrier for the oxidation degradation process of HCHO on the Ni–MoS_2 surface, it is imperative the van der Waals to incorporate the DFT-3 correction.[51] The influence of spin polarization on the structure is taken into account during the process of structural optimization to verify the impact from the magnetic atom Ni. However, calculations indicate that Ni does not exhibit magnetism in this system. Therefore, further discussion will not explore the influence of magnetism.

To achieve a balance between calculation accuracy and efficiency, MoS_2 of the $2\sqrt{3} \times 2\sqrt{3} \times 1$ model is employed with a 20 Å vacuum along the z axis (perpendicular to the interface) to prevent any artificial interactions among repeated slabs. The Brillouin zone (BZ) is sampled by using a $5 \times 5 \times 1$ Γ-centered Monkhorst–Pack grid.[52] Atomic relaxation is performed until the Hellmann–Feynman force on each atom is less than 0.03 eV $Å^{-1}$.

The CI-NEB method is an enhanced version of the NEB method, wherein the image corresponding to the highest energy is shifted towards the saddle point position. Consequently, this approach exhibits superior computational efficiency and yields more precise outcomes. Upon convergence of the climbing image nudged elastic band (CINEB), the structure possessing the highest energy represents the transition state structure.[53] To obtain precise transition state images while conserving computing resources, a loose convergence standard of 0.1 eV Å^{-1} is employed for the preliminary transition state graph search using the CINEB method.[54] This method, however, still entails a significant consumption of computational resources and time. Subsequently, the improved dimer method (IDM)[55] is utilized to determine the structure of the transition state until the force per atom falls below 0.05 eV Å^{-1}. The total energy change of each process of atomic relaxation and the transition state search is less than 10^{-6} eV. Finally, frequency analysis is conducted on the transition state image to ensure its accuracy.

The adsorption energy (E_{ads}) is calculated using the following equation

$$E_{ads} = E_{abs} - E_{group} \quad (1)$$

where E_{ads} is the energy of the adsorption system and E_{ads} and E_{group} are the energy of the Ni–MoS_2 abstract and the molecular group on the surface.

The energy barrier (E_b) and reaction heat (ΔE) of the reaction process are calculated using the following formulas

$$E_b = E_{TS} - E_{IS} \quad (2)$$

$$\Delta E = E_{IM} - E_{IS} \quad (3)$$

where E_{IS}, E_{IM} and E_{TS} represent the energy of the initial state, intermediate state and transition state in a reaction path, respectively.

Formula (4) is employed to calculate the heat of the reaction based on the variation in Gibbs free energy (ΔG), enabling a thermodynamic analysis of the reaction pathway.

$$\Delta G = G_{FS} - G_{IS} \quad (4)$$

G_{FS} and G_{IS} demonstrate the variation of Gibbs free energy between the initial and final states, respectively.

The relevant parameters for thermodynamics analysis are computed utilizing formula

$$\Delta G = -RT\mathrm{Ln}\,K \Leftrightarrow \mathrm{Ln}\,K = \frac{-\Delta G}{RT} \quad (5)$$

where ΔG is the Gibbs free energy difference between the FS state and TS0 state, R denotes the ideal gas constant, T represents the thermodynamic temperature, and K signifies the equilibrium constant of the reaction.

The relevant parameters for dynamic analysis are computed utilizing formula

$$K^{TST} = \frac{k_B T}{h} \times \exp\left(\frac{-\Delta G_b}{k_B T}\right) \quad (6)$$

where k_B and h are the Boltzmann constant and Planck constant, respectively; T is the reaction temperature under study; and G_b is the reaction barrier in terms of Gibbs free energy.

3. Results and discussion

The optimized model of Ni–MoS_2 and the image of unfolded band structures are illustrated in Fig. 1, wherein the Ni atom is anchored by three S atoms atop the Mo atom, thereby forming an exposed active site. In comparison to the MoS_2 surface, the Ni atom exhibits a vertical displacement of 0.99 Å, which serves as a favorable molecular anchor point. Furthermore, the bond length between Ni and the three S atoms is 2.12 Å. The pristine MoS_2 monolayer exhibits behavior of a direct band-gap semiconductor. By comparing the unfolded band structures (see Fig. S1, ESI†), it can be seen that the orbital hybridization between Ni and neighboring S atoms leads to the enhancement of orbital delocalization around the valence band edge. Meanwhile, the metal Ni atom as a donor defect introduces net electrons into the system, resulting in the Fermi level moving to the conduction band edge, which conforms to the characteristics of semiconductor n-type doping.

The prerequisite for achieving efficient catalytic oxidation lies in the establishment of stable adsorption of relevant gases

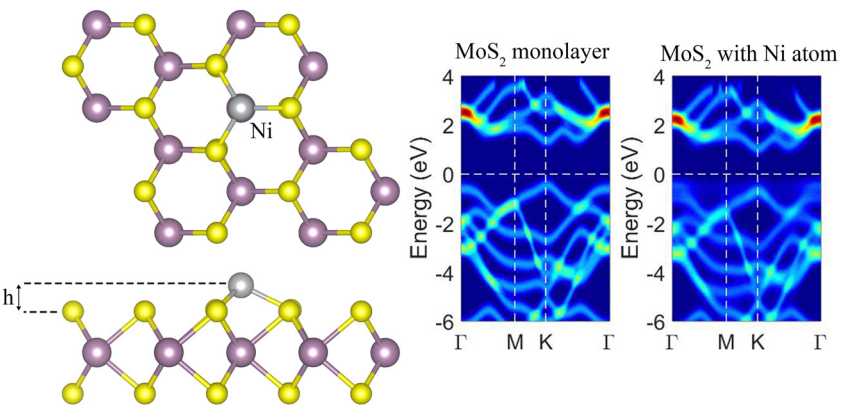

Fig. 1 The optimized model of Ni–MoS_2 and the image of unfolded band structures.

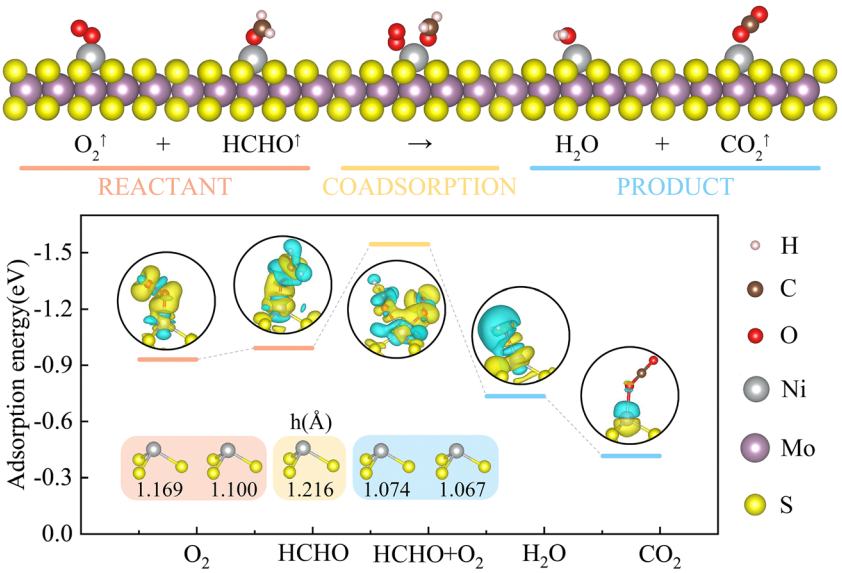

Fig. 2 The adsorption model of gas molecules related to Ni–MoS_2 on the surface and the corresponding variations in adsorption energy and Ni atom height.

on the catalyst surface. Therefore, our initial focus is to investigate the adsorption characteristics of reactants and products involved in the oxidative degradation of HCHO on Ni–MoS_2, including individual adsorptions of O_2, HCHO, H_2O, and CO_2 on Ni–MoS_2, as well as simultaneous adsorptions of O_2 and HCHO. The adsorption structure model and the key parameters are illustrated in Fig. 2. The electron density difference plot corresponding to the relevant structures is illustrated in Fig. S2 (ESI†). The adsorption energies of Ni–MoS_2 for the reactants O_2 and HCHO are 0.93 eV and 0.99 eV, respectively. At the interface between Ni and the reactant molecules, electron transfer occurs resulting in stable adsorption on the exposed Ni site, thereby leading to an increased distance between Ni and the MoS_2 surfaces. The adsorption energies of H_2O and CO_2, the oxidation products catalyzed by HCHO, on the Ni–MoS_2 surface are 0.73 eV and 0.41 eV, respectively, which are significantly lower than those of the reactants. Therefore, the decomposition products can be rapidly separated from the catalyst surface to prevent their accumulation and blockage of active sites that would reduce catalytic activity. This is conducive to achieving a rapid and efficient catalytic reaction while improving HCHO removal rates. The co-adsorption model of O_2 and HCHO at the Ni site demonstrates an adsorption energy of 1.55 eV, resulting in a height increase of the Ni atom to 1.216 Å, which is 22.5% higher compared to the absence of adsorbed molecules. In contrast to individual O_2 or HCHO adsorption, co-adsorption on Ni–MoS_2 significantly enhances both the adsorption energy and the relative height of Ni atoms, indicating that the co-adsorption model provides enhanced stability and promotes the initiation of catalytic reactions.

Based on the analysis of reactants and products, the initial configuration of the Ni–MoS_2 surface catalytic degradation of HCHO can be determined. Given that the adsorption energy of co-adsorbed O_2 and HCHO is significantly higher than that of HCHO alone, the co-adsorption model is selected as one of the initial reaction configurations. In the co-adsorption configuration, the length of the O–O bond is 1.29 Å, which exceeds that of gas phase O_2 at 1.21 Å, indicating partial activation during co-adsorption. This initial configuration adheres to the Langmuir–Hinshelwood (L–H) reaction mechanism. Considering both the strong adsorption capacity of Ni–MoS_2 for O_2 and the typically lower concentration levels of HCHO under ambient conditions compared to those of O_2 in general, free HCHO and activated O_2 on the surface are also examined as reasonable initial configurations within an Eley–Rideal (E–R) mechanism framework. In this E–R mechanism scenario, an elongated O–O bond by 0.1 Å activates O_2 further. Due to complexities associated with different catalyst surfaces decomposition pathways for converting HCHO into CO_2 and H_2O, in the study conducted by Bai *et al.*, a three-dimensional mesoporous Ag/Co_3O_4 catalyst was employed for the oxidative degradation of HCHO,[56] while Zhang *et al.* reported a high-efficiency catalytic process of HCHO at room temperature using Pt/TiO_2,[57] only two common paths for CO_2 and H_2O generation within L–H and E–R mechanisms are analyzed extensively in this study.

The corresponding reaction pathways of the L–H and E–R mechanisms are illustrated in Fig. 3. In the L–H mechanism, both reaction paths originate from the initial state IS1. Along the first path, the O atom situated further away from the Ni–MoS_2 surface in O_2 is attracted to the C atom in HCHO, resulting in stretching of the O–O bond length from 1.29 Å at IS1 to 1.38 Å (TS1), thereby weakening their interaction. Consequently, a 5-membered intermediate peroxide ring (IM1) is formed. This process has an energy barrier of 1.78 eV while absorbing 0.17 eV of heat. Due to its unstable structure, during rotation of this newly generated species, continuous stretching of the O–O bond occurs until it eventually breaks (TS2), one of

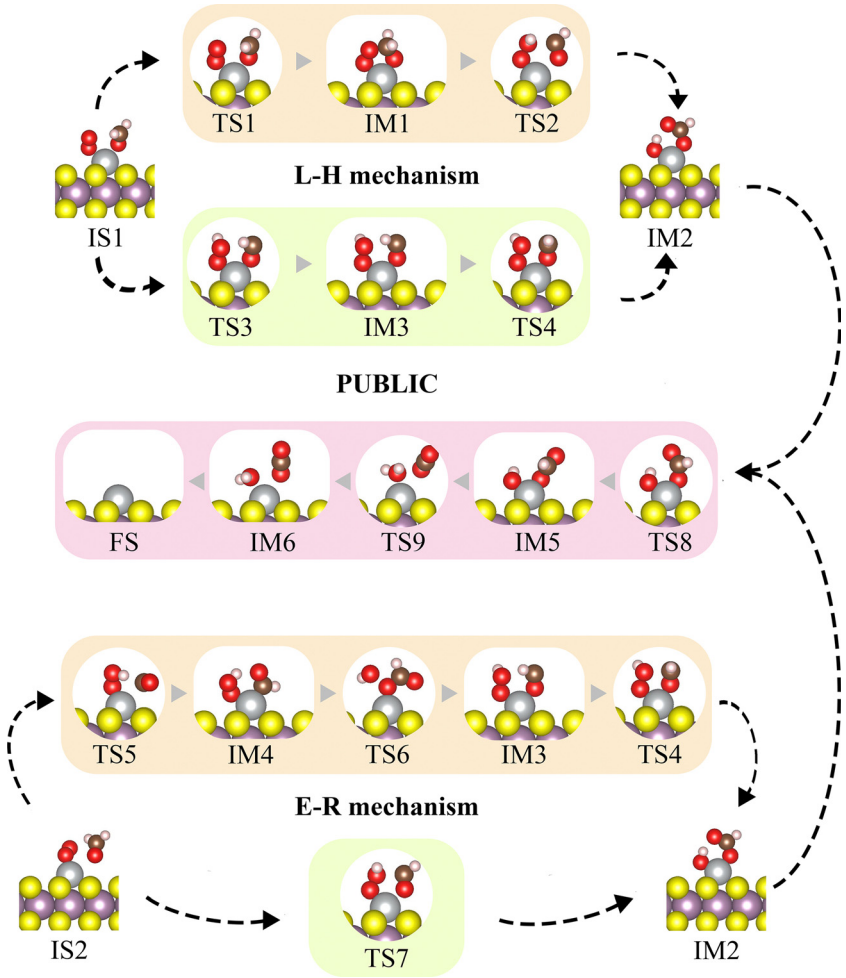

Fig. 3 The reaction path corresponds to the intermediate state and transition state model.

the H atoms transfers to an O atom, forming structures comprising OH^- and $HCOO^-$ groups (IM2). The energy barrier for this step amounts to 1.32 eV with a heat release of 2.92 eV. The OH^- group and the $HCOO^-$ group are continuously rotating, with the $HCOO^-$ group undergoing a reversal process that brings the H atom closer to OH^- (as shown in TS8), resulting in the formation of IM5. Throughout this process, the energy barrier associated with group rotation adjusts its configuration to 0.15 eV, leading to an energy reduction of IM5 by 0.16 eV. Subsequently, H departs from the $HCOO^-$ group and combines with OH^- to generate CO_2 and H_2O (TS9). The occurrence of this step is accompanied by a minute energy barrier of 0.02 eV, while simultaneously releasing 1.54 eV of heat. Ultimately, the final products of the catalytic reaction H_2O and CO_2, merely necessitate surpassing an energy barrier of 0.71 eV for dissociation from the Ni–MoS_2 surface (IM6 to FS). The rate-determining step for this pathway lies between IS1 and IM1, which represents the highest energy barrier within the first reaction pathway. In the second reaction pathway of the same mechanism, there is a direct transfer between the H atom in HCHO and adsorbed O_2. This process enhances Ni–O interaction, leading to a shortened Ni–O bond length from 1.99 Å (IS1) to 1.87 Å (TS3). Additionally, it weakens the O–O interaction as evidenced by a 0.16 Å increase in the O–O bond length; meanwhile, this process exhibits an energy barrier of 1.36 eV with a corresponding reduction in IM3 energy by 0.33 eV. The newly formed groups continue rotating and colliding as they stretch and break O–O bonds while forming new C–O bonds simultaneously (see TS4), eventually resulting in the deposition of the H atom onto the remaining O atoms to form an identical IM2 structure observed in path one. The energy barrier of this process is 0.88 eV with 2.41 eV energy released. And the following steps of this process are consistent with those described previously. In this particular path, the speed determination step represents the highest energy barrier encountered when transitioning from IS1 to IM3. For both reaction paths operating under the L–H mechanism, the formation route involving the generation of $OOH^-$and HCO^- groups experiences a decreased energy barrier by approximately 0.66 eV compared to that involving formation *via* the creation of an intermediate peroxide ring.

The L–R mechanism involves two common reaction paths, and the initial configurations of these paths are depicted in IS2. In the first path, the C–H bond in the HCHO molecule

undergoes cleavage, resulting in the formation of an OOH^- group (as illustrated in TS5). HCO^- groups form Ni–C bonds with Ni. This process only requires overcoming a reaction energy barrier of 0.02 eV while releasing 0.2 eV of thermal energy. Subsequently, the HCO^- group continues to rotate until the Ni–C bond breaks and a newly formed Ni–O bond is established (TS6 to IM3). Accomplishing this step necessitates surpassing an energy barrier of 1.29 eV while simultaneously releasing 0.13 eV of heat. Further rotation and collision between the HCO^- group and OOH^- group lead to the formation of an IM2 structure upon breaking of the O–O bond. This particular step demands overcoming a barrier of 0.88 eV while the heat of the reaction released is 2.4 eV. For the second reaction pathway of the L–R mechanism, following the collision between free HCHO and O_2, the HCO^- group undergoes a transition state similar to that observed in the IM3 process (see TS7) during rotation before reaching the IM2 state. This process necessitates overcoming an energy barrier of 1.26 eV while releasing 2.74 eV of heat. Subsequently, the reaction pathway in the IM2 state follows as described above. In reaction pathways of the L–R mechanism, the highest energy barrier occurs at the step between IM4 to IM3 (1.29 eV) and IS2 to IM2 (1.26 eV), these are rate-determining steps of the L–R mechanism. Furthermore, for these two L–R mechanism reaction pathways, adjusting the adsorption position of the HCO^- group after dissociation requires a higher energy barrier compared to directly adjusting the adsorption position during collision. However, due to its lower energy barrier required for collision dissociation, PATH1 is more likely to occur than PATH2 when HCHO collides with O_2 initially. Nevertheless, completing subsequent adjustment of adsorption site necessitates overcoming an even larger energy barrier. Hence, within the L–R mechanism, one of the pathways exhibits a favorable initiation while the other demonstrates an advantageous propulsion.

To facilitate a more intuitive comparison of Gibbs free energy variation trends across the four reaction paths, in Fig. 4, the free energy variation trends of the four reaction paths investigated in this study are graphically represented based on the free energy mapping of ΔG of each configuration. IS1 and IS2 denote initial states for L–H and E–R mechanisms, respectively, with little difference observed in their respective free energies (−303.854 eV and −303.855 eV). The present study investigates four reaction pathways, two of which originate from IS1 and the other two from IS2, all of which share a common reaction pathway PUBLIC (IM2 → TS8 → IM5 → TS9 → IM6 → FS), the highest energy barrier in this local pathway is 0.71 eV in the process of H_2O and CO_2 desorption. The L–H mechanism exhibits a maximum free energy barrier of 1.78 eV along PATH1 during the IS1 → IM1 process, this is the highest free energy barrier among all processes, the other three pathways have their maximum free energy barriers of 1.36 eV, 1.29 eV and 1.26 eV, respectively.

Comparing the two reaction pathways in the L–H mechanism, it is evident that the energy barrier for IS1 → TS1 is significantly higher (1.78 eV) compared to IS1 → TS3 (1.36 eV). Therefore, in comparison to the formation of an unstable 5-member peroxide ring, the peroxide ring undergoes rotational cleavage resulting in the generation of OOH^- and CHO^- groups. The catalytic reaction exhibits a greater propensity for direct C–H bond cleavage in HCHO, leading to the formation of OOH^- and CHO^- groups. This provides a competitive advantage for PATH2. Comparing the initial step processes of the two reaction pathways in the E–R mechanism, it is observed that PATH1 exhibits a significantly lower energy barrier of only 0.02 eV for its first step reaction, whereas PATH2 presents a higher energy barrier of 1.26 eV for its first step reaction. Consequently, PATH1 may possess certain advantages in terms of reactivity. However, it should be noted that PATH1 encounters an additional energy barrier of 1.29 eV in the second step, which could potentially result in a lower actual reaction rate compared to that of PATH2. All four pathways exhibit similar behavior during H_2O and CO_2 desorption by overcoming a dissociation energy barrier of 0.71 eV effectively, thereby facilitating product desorption and preventing active site blockage.

Compared to other relevant research findings, according to Ding *et al.*,[58] the energy barrier for the speed determination process of Pt/TiO_2 during HCHO oxidation is 230.45 KJ mol^{-1} (approximately 2.04 eV). Liu *et al.*, in their investigation on the oxidation pathway of HCHO on $Fe/DV\text{-}N_4$ and $Pd/DV\text{-}N_4$ surfaces,[59] observed significantly higher reaction energy barriers of 2.63 eV and 6.08 eV, respectively. These values exceed the response path obtained in our study. The oxidation mechanism of HCHO on Algraphene at room temperature was investigated by Liu *et al.*,[60] and their study reported a lower energy barrier of 0.82 eV compared to this study. However, the dissociation energy of the reaction product in their study is found

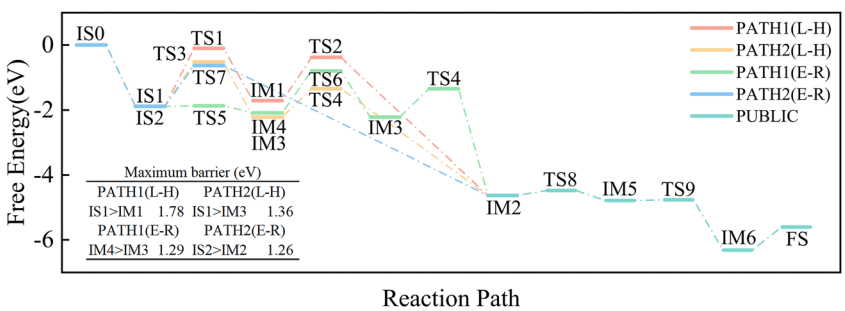

Fig. 4 The total Gibbs free energy map and the maximum barrier of each reaction path.

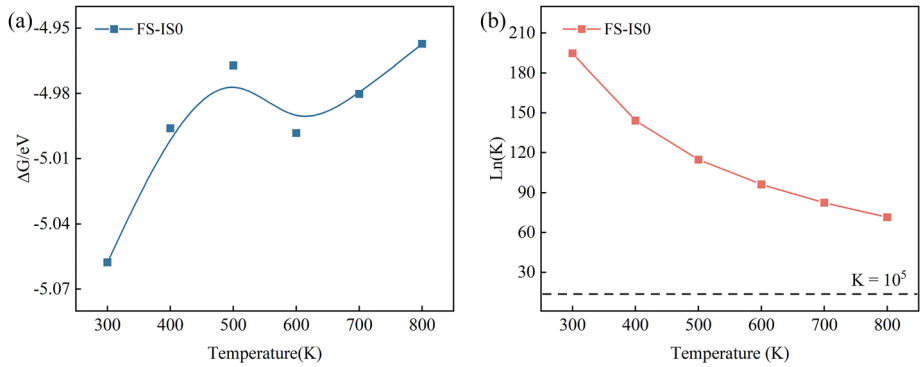

Fig. 5 (a) The free reaction energy and (b) the logarithms of reaction equilibrium constants at various temperatures.

to be significantly larger and more challenging to dissociate. Therefore, Ni–MoS_2 exhibits great potential and high research value in the field of catalytic oxidation of HCHO.

In order to further investigate the thermodynamic properties of the oxidative degradation process of HCHO on a Ni–MoS_2 surface, we utilized free reaction energy and reaction equilibrium constants at various temperatures to assess the thermodynamic characteristics of the process across different temperature ranges. Considering the temperature range observed in the laboratory for the oxidative degradation process of HCHO, this study focuses on investigating the free reaction energy and reaction equilibrium constant within the range of 300–800 K. In Fig. 5, logarithms are applied to the calculated free reaction energy and reaction equilibrium constant, which are then plotted with ΔG serving as a basis for energy mapping to visually demonstrate the spontaneity and equilibrium laws of reactions at different temperatures.

The reaction energy of the catalytic degradation process of HCHO, as depicted in Fig. 5(a), is consistently negative within the temperature range investigated in this study, indicating that the reaction occurs spontaneously under these conditions. The increase in temperature leads to a corresponding rise in reaction energy, thereby impeding the catalytic degradation of HCHO on the surface of Ni–MoS_2. The catalytic degradation process of HCHO on the surface of Ni–MoS_2 is a completely irreversible reaction, the significantly higher reaction equilibrium constant ($>10^5$) within the temperature range of 300–800 K serves as evidence, indicating that HCHO is oxidatively degraded to CO_2 and H_2O. Moreover, in Fig. 5(b), an increase in temperature leads to a gradual decrease in the reaction equilibrium constant, suggesting that the oxidative degradation of HCHO is generally exothermic.

Subsequently, in order to gain further insights into the kinetic characteristics of the catalytic degradation reaction of HCHO on the surface of Ni–MoS_2, we focused our research on determining the rate-limiting steps in each reaction pathway based on the aforementioned analysis of the reaction process. Specifically, for the L–H mechanism, IS1 to IM1 and IS1 to IM3 are selected; whereas for the E–R mechanism, IM4 to IM3 and IS2 to IM2 are chosen. The reaction rate constant of the speed determination step is calculated using formula (6), as illustrated in Fig. 6. Ln(K^{TST}) is plotted on the y-axis and 1000/T on the x-axis for ease of analysis.

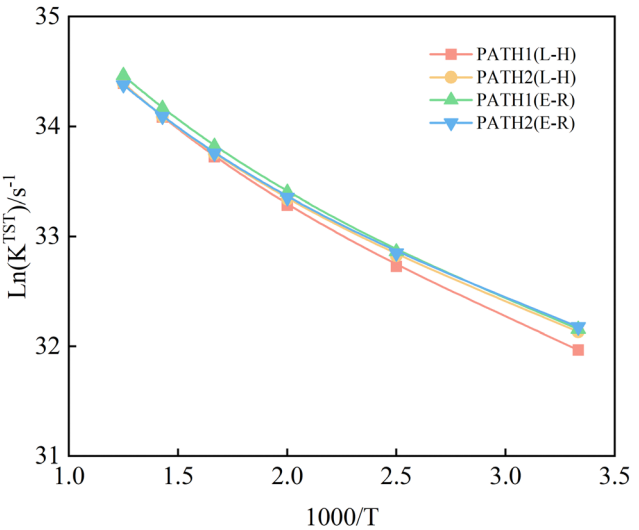

Fig. 6 The logarithms of the reaction rate constants for the rate-determining steps in each pathway at various temperatures.

The reaction rate constant curves for the velocity determination steps correspond to the four reaction paths, as depicted in Fig. 6, the slope of all the curves consistently exhibits a negative trend, indicating that an increase in temperature promotes the catalytic degradation of HCHO. Moreover, it is observed that the reaction rate constants for all four reaction paths demonstrate similar variations in temperature and remain positive within the range of 300–800 K. The temperature range is expanded to 100–800 K in order to further elucidate the correlation between the catalytic degradation rate of HCHO on the surface of Ni–MoS_2 and temperature, relevant information can be found in Table S1 (ESI†). When the temperature drops to 100 K, the reaction rate constants of the four pathways exhibit a significant decrease; however, they still remain above 27.9. Hence, it can be inferred that Ni–MoS_2 retains its effectiveness as a catalyst for HCHO degradation even under extreme temperature conditions, thereby demonstrating its potential catalytic properties in such scenarios. The effective

Table 1 The rate determining step for each pathway involves the pre-exponential factor (A) and activation energy (E_a)

PATH	E_a (eV)	A (s^{-1})
L–H (PATH1)	1.03	3.21×10^{15}
L–H (PATH2)	0.93	2.87×10^{15}
E–R (PATH1)	0.95	3.22×10^{15}
E–R (PATH2)	0.91	2.77×10^{15}

collision frequency between the reactant molecules and the catalyst surface decreases at low temperatures, and the dissociation difficulty of the product increases. Maintaining optimal catalyst performance under such conditions remains a significant challenge for low temperature catalysts. However, this study highlights the potential of Ni–MoS_2 for efficient formaldehyde degradation at low temperatures, warranting further exploration.

In addition, Arrhenius parameters of the speed determination steps of the four paths are obtained by linear fitting, as shown in Table 1. The activation energies of the four paths differ little (0.91 eV to 1.03 eV). The temperature range covered in this paper exhibits a relatively high rate of PATH2 reactions in both the E–R mechanism and the L–H mechanism, indicating its higher likelihood of occurrence. Due to the high energy barrier of the initial step, PATH1 in the L–H pathway is relatively challenging to occur. However, within the temperature range discussed in this paper, the activation energy for all four pathways is comparatively low, ensuring a certain reaction rate regardless of which catalytic reaction path is undertaken. Nevertheless, HCHO oxidation is most favorably facilitated by PATH2 in the E–R mechanism. The final products of the four reaction pathways, namely H_2O and CO_2, only require overcoming a low energy barrier of 0.71 eV for desorption on the surface of Ni–MoS_2. This favorable energy barrier facilitates easy desorption of catalytic products from the surface, promoting efficient reaction cycles and catalyst reuse. Based on this analysis, it can be concluded that Ni–MoS_2 is a promising HCHO catalyst with significant potential under extreme conditions.

4. Conclusions

The oxidative degradation mechanism of HCHO on the surface of Ni–MoS_2 is investigated using the DFT method. The reaction pathways for the L–H and E–R mechanisms are thoroughly examined. The energy barriers for each step are calculated to determine the rate-determining steps in each pathway. The kinetics and thermodynamics of HCHO degradation on the Ni–MoS_2 surface at different temperatures are studied to understand the law of equilibrium constant and reaction rate. In this study, two L–H and two E–R reaction pathways are selected for investigation. All four pathways can occur spontaneously and irreversibly within a temperature range from 300 K to 800 K, while still maintaining a certain reaction rate even at 100 K. Moreover, the activation energy for HCHO oxidation on the Ni–MoS_2 surface ranges from 0.91 eV to 1.03 eV, with one dominant path in the E–R mechanism having a first-step energy barrier as low as 0.02 eV; another E–R mechanism exhibits the lowest activation energy overall. Therefore, it is speculated that the E–R mechanism may play a predominant role in the catalytic degradation processes of HCHO. The oxidative degradation of HCHO leading to final products H_2O and CO_2 only requires overcoming a desorption energy barrier of 0.71 eV, which is advantageous due to its low value. The aforementioned research and analysis demonstrate that Ni–MoS_2 holds great potential as a catalyst for indoor environment or extreme temperature environment applications in HCHO oxidative degradation.

Conflicts of interest

The authors declare no competing financial interest.

Acknowledgements

This work was partially supported by the National Natural Science Foundation of China (No. 11704282), the Natural Science Foundation of Tianjin City (No. 18JCQNJC72900), and the Graduate Science and Innovation Project of Tianjin University of Technology (No. YJ2313).

References

1 J. Thrane, U. V. Mentzel, M. Thorhauge, M. Høj and A. D. Jensen, *Catalysts*, 2021, **11**, 1329.
2 T. Brown, C. Dassonville, M. Derbez, O. Ramalho, S. Kirchner, D. Crump and C. Mandin, *Environ. Res.*, 2015, **140**, 385–396.
3 J. Xiong, P. Zhang, S. Huang and Y. Zhang, *Environ. Res.*, 2016, **151**, 734–741.
4 M. Hauptmann, J. H. Lubin, P. A. Stewart, R. B. Hayes and A. Blair, *Am. J. Epidemiol.*, 2004, **159**, 1117–1130.
5 M. Z. M. Salem and M. Bohm, *BioResources*, 2013, **8**, 4775–4790.
6 T. Salthammer, S. Mentese and R. Marutzky, *Chem. Rev.*, 2010, **110**, 2536–2572.
7 T. Zinn, D. Cline and W. F. Lehmann, *For. Prod. J.*, 1990, **40**, 15–18.
8 N. E. Klepeis, W. C. Nelson, W. R. Ott, J. P. Robinson, A. M. Tsang, P. Switzer, J. V. Behar, S. C. Hern and W. H. Engelmann, *J. Exposure Anal. Environ. Epidemiol.*, 2001, **11**, 231–252.
9 J. J. Collins and G. A. Lineker, *Regul. Toxicol. Pharmacol.*, 2004, **40**, 81–91.
10 S. Duhayon, P. Hoet, G. Van Maele-Fabry and D. Lison, *Int. Arch. Occup. Environ. Health*, 2008, **81**, 695–710.
11 J. Ye, Y. Yu, J. Fan, B. Cheng, J. Yu and W. Ho, *Environ. Sci.: Nano*, 2020, **7**, 3655–3709.
12 H. Chen, J. He, C. Zhang and H. He, *J. Phys. Chem. C*, 2007, **111**, 18033–18038.
13 M. H. Sherman and A. T. Hodgson, *Indoor Air*, 2004, **14**(1), 2–8.

14 E. Roffael, *Formaldehyde Release from Particleboard and Other Wood Based Panel*, Forest Research Institute Malaysia, Kuala Lumpur, 1993.
15 M. Dunky and P. Niemz, in *Holzwerkstoffe und Leime: Technologie und Einflussfaktoren*, ed. M. Dunky and P. Niemz, Springer Berlin Heidelberg, Berlin, Heidelberg, 2002, pp. 573–614.
16 Q. Ye, J. E. Krechmer, J. D. Shutter, V. P. Barber, Y. Li, E. Helstrom, L. J. Franco, J. L. Cox, A. I. H. Hrdina, M. B. Goss, N. Tahsini, M. Canagaratna, F. N. Keutsch and J. H. Kroll, *Environ. Sci. Technol. Lett.*, 2021, **8**, 1020–1025.
17 Q. L. Yu and H. J. H. Brouwers, *Appl. Catal., B*, 2009, **92**, 454–461.
18 M. R. Hoffmann, S. T. Martin, W. Choi and D. W. Bahnemann, *Chem. Rev.*, 1995, **95**, 69–96.
19 J. P. Ghosh, G. Achari and C. H. Langford, *Water Environ. Res.*, 2016, **88**(8), 785–791.
20 T. Salthammer and F. Fuhrmann, *Environ. Sci. Technol.*, 2007, **41**, 6573–6578.
21 L. Benz, J. Haubrich, R. G. Quiller, S. C. Jensen and C. M. Friend, *J. Am. Chem. Soc.*, 2009, **131**(41), 15026–15031.
22 H. Schmitz, U. Hilgers and M. Weidner, *New Phytol.*, 2000, **147**, 307–315.
23 T. Godish and C. Guindon, *Environ. Pollut.*, 1989, **62**, 13–20.
24 L. Miao, J. Wang and P. Zhang, *Appl. Surf. Sci.*, 2019, **466**, 441–453.
25 J. Gong, S. Rong, X. Wang and Y. Zhou, *J. Cleaner Prod.*, 2022, **377**, 134242.
26 B. Bai, Q. Qiao, J. Li and J. Hao, *Chin. J. Catal.*, 2016, **37**, 102–122.
27 N. Liu, K. Kourtakis, J. C. Figueroa and J. G. Chen, *J. Catal.*, 2003, **215**, 254–263.
28 K. Habermehl-Ćwirzeń, J. Lahtinen and P. Hautojärvi, *Surf. Sci.*, 2005, **598**, 128–135.
29 L. Shi, Q. Li, C. Ling, Y. Zhang, Y. Ouyang, X. Bai and J. Wang, *J. Mater. Chem. A*, 2019, **7**, 4865–4871.
30 Z. Xu, R. Fan, X. Zhou, G. Huang, X. Wu and M. Shen, *ACS Sustainable Chem. Eng.*, 2019, **7**, 19832–19838.
31 X. Zhang, Q. W. Zhang, Y. F. Sun and J. X. Guo, *Fuel*, 2016, **184**, 559–564.
32 X. Li, L. Zhang, X. B. Zang, X. M. Li and H. W. Zhu, *ACS Appl. Mater. Interfaces*, 2016, **8**, 10866–10873.
33 B. Chen, T. S. Wang, S. Y. Zhao, J. Y. Tan, N. Q. Zhao, S. P. Jiang, Q. F. Zhang, G. M. Zhou and H. M. Cheng, *Adv. Mater.*, 2021, **33**, e2007090.
34 J. Deng, H. B. Li, J. P. Xiao, Y. C. Tu, D. H. Deng, H. X. Yang, H. F. Tian, J. Q. Li, P. J. Ren and X. H. Bao, *Energy Environ. Sci.*, 2015, **8**, 1594–1601.
35 B. T. Qiao, A. Q. Wang, X. F. Yang, L. F. Allard, Z. Jiang, Y. T. Cui, J. Y. Liu, J. Li and T. Zhang, *Nat. Chem.*, 2011, **3**, 634–641.
36 L. Guo, R. Li, J. Jiang, X. Fan, J.-J. Zou and W. Mi, *Appl. Surf. Sci.*, 2022, **599**, 153979.
37 Z. C. Zhuang, Y. H. Li, R. H. Yu, L. X. Xia, J. R. Yang, Z. Q. Lang, J. X. Zhu, J. Z. Huang, J. O. Wang, Y. Wang, L. D. Fan, J. S. Wu, Y. Zhao, D. S. Wang and Y. D. Li, *Nat. Catal.*, 2022, **5**, 300–310.
38 H. Zhou, Y. F. Zhao, J. Xu, H. R. Sun, Z. J. Li, W. Liu, T. W. Yuan, X. Q. Wang, W. O. Cheong, Z. Y. Wang, X. Wang, C. Zhao, Y. C. Yao, W. Y. Wang, F. Y. Zhou, M. Chen, B. J. Jin, R. B. Sun, J. Liu, X. Hong, T. Yao, S. Q. Wei, J. Luo and Y. E. Wu, *Nat. Commun.*, 2020, **11**, 335.
39 Y. Lei, D. Butler, M. C. Lucking, F. Zhang, T. N. Xia, K. Fujisawa, T. Granzier-Nakajima, R. Cruz-Silva, M. Endo, H. Terrones, M. Terrones and A. Ebrahimi, *Sci. Adv.*, 2020, **6**, eabc4250.
40 X. Sun, C. Chen, C. Xiong, C. Zhang, X. Zheng, J. Wang, X. Gao, Z.-Q. Yu. and Y. Wu, *Nano Res.*, 2023, **16**, 917–924.
41 Y. Hao, Y.-T. Wang, L.-C. Xu, Z. Yang, R.-P. Liu and X.-Y. Li, *Appl. Surf. Sci.*, 2019, **469**, 292–297.
42 X. Hai, S. Xi, S. Mitchell, K. Harrath, H. Xu, D. F. Akl, D. Kong, J. Li, Z. Li, T. Sun, H. Yang, Y. Cui, C. Su, X. Zhao, J. Li, J. Pérez-Ramírez and J. Lu, *Nat. Nanotechnol.*, 2022, **17**, 174–181.
43 J. P. Perdew, K. Burke and M. Ernzerhof, *Phys. Rev. Lett.*, 1996, **77**, 3865–3868.
44 G. Kresse and J. Furthmüller, *Phys. Rev. B: Condens. Matter Mater. Phys.*, 1996, **54**, 11169–11186.
45 G. Kresse and D. Joubert, *Phys. Rev. B: Condens. Matter Mater. Phys.*, 1999, **59**, 1758–1775.
46 R. M. Martin, *Electronic structure: basic theory and practical methods*, Cambridge university press, Cambridge, 2020.
47 Y. Liu, M. Ren, B. Song and M. Dong, *Appl. Surf. Sci.*, 2023, 622.
48 Q. Liu, H. Cheng, X. Wang and P. Qian, *Phys. Chem. Chem. Phys.*, 2023, **25**, 5056–5065.
49 H. Zhang, Y. Ma, H. Xiong, G. Deng, L. Yang and Z. Nie, *Surf. Interfaces*, 2023, 36.
50 J. Hafner, *J. Comput. Chem.*, 2008, **29**, 2044–2078.
51 S. Grimme, J. Antony, S. Ehrlich and H. Krieg, *J. Chem. Phys.*, 2010, **132**, 154104.
52 H. J. Monkhorst and J. D. Pack, *Phys. Rev. B: Solid State*, 1976, **13**, 5188–5192.
53 G. A. Henkelman, B. P. Uberuaga and H. Jónsson, *J. Chem. Phys.*, 2000, **113**, 9901–9904.
54 G. Henkelman, B. P. Uberuaga and H. Jonsson, *J. Chem. Phys.*, 2000, **113**, 9901–9904.
55 A. Heyden, A. T. Bell and F. J. Keil, *J. Chem. Phys.*, 2005, **123**, 224101.
56 B. Bai and J. Li, *ACS Catal.*, 2014, **4**, 2753–2762.
57 C. Zhang, H. He and K.-I. Tanaka, *Catal. Commun.*, 2005, **6**, 211–214.
58 J. Ding, Y. Yang, J. Liu and Z. Wang, *Chemosphere*, 2020, **248**, 125980.
59 S. T. Liu, S. L. Niu, J. W. Liu, D. Wang, Y. Z. Wang and K. H. Han, *Mol. Catal.*, 2022, **528**, 112516.
60 G. Liu, J. Zhou, W. Zhao, Z. Ao and T. An, *Chin. Chem. Lett.*, 2020, **31**, 1966–1969.

